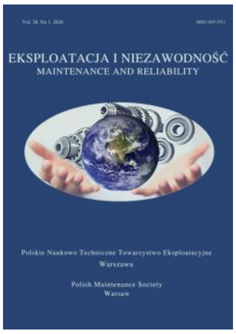

Eksploatacja i Niezawodnosc – Maintenance and Reliability

Volume 28 (2026), Issue 1

journal homepage: http://www.ein.org.pl

Article citation info:
Zhi S, Niu Y, Ma L, Wu H, Shen H, Wang T, Local Entropy Selection Scaling-extracting Chirplet Transform for Enhanced Time-Frequency Analysis and Precise State Estimation in Reliability-Focused Fault Diagnosis of Non-stationary Signals, Eksploatacja i Niezawodnosc – Maintenance and Reliability 2026: 28(1) http://doi.org/10.17531/ein/205977

Local Entropy Selection Scaling-extracting Chirplet Transform for Enhanced Time-Frequency Analysis and Precise State Estimation in Reliability-Focused Fault Diagnosis of Non-stationary Signals

Indexed by: Web of Science Group

Shaodan Zhi[a], Yuli Niu[b], Limei Ma[b], Hengshan Wu[a], Haikuo Shen[a], Tianyang Wang[c,*]

[a] Beijing Jiaotong University, China
[b] Beijing Institute of Petrochemical Technology, China
[c] Tsinghua University, China

Highlights

- LESSECT enhances time-frequency resolution for non-stationary signals.
- LESSECT excels in resolving closely spaced, non-proportional instantaneous frequencies.
- LESSECT overcomes energy leakage and blurring issues in traditional TFA techniques.
- LESSECT improves the reliability of fault detection in rotating machinery systems.

Abstract

Under diverse conditions, the vibration signals of complex rotating machinery exhibit non-stationary behavior, multi-component characteristics, closely spaced frequencies, and non-proportionality, posing challenges to conventional time-frequency analysis (TFA) methods. These limitations hinder accurate instantaneous frequency (IF) estimation and time-frequency representation (TFR) construction, directly impacting machinery fault diagnosis. As such, we propose the Local Entropy Selection Scaling-Extracting Chirplet Transform (LESSECT), which optimizes entropy-based chirp rate (CR) selection to match non-proportional fundamental frequencies. By adaptively selecting multiple CRs at the same time center, LESSECT enhances TFR resolution and energy concentration, leading accurate IF identification. Experimental validation on bat echolocation, bearing fault, and planetary gearbox signals shows its superior performance in resolving non-proportional, closely spaced IFs. This significantly improves state estimation and enhances machinery diagnostics, contributing to greater system reliability.

Keywords
non-stationary signals, time-frequency analysis, non-proportional instantaneous frequency, fault diagnosis, system reliability

1. Introduction

Vibration signals in complex rotating machinery under time-varying operating conditions exhibit non-stationary, multi-component, and non-proportional characteristics, posing significant challenges for signal processing and data analysis. The accuracy and precision of these analyses are crucial for assessing the health status and detecting faults in rotating machinery, directly impacting the system's reliability and performance [1-3]. Reliable fault detection is essential to prevent catastrophic failures and ensure the continuous, efficient operation of machinery [4,5]. Therefore, the study of such signals has gained significant attention in the domain of reliability-centered fault detection and health monitoring [6-11].

In recent years, data-driven fault diagnosis methods, particularly those based on machine learning and deep learning, have emerged as powerful tools for identifying fault patterns and extracting meaningful features from vibration signals.

(*) Corresponding author.
E-mail addresses: S. Zhi (ORCID: 0000-0001-5898-3992) sdzhi@bjtu.edu.cn, Y. Niu (ORCID: 0009-0005-1349-2491) 2022520093@bipt.edu.cn, L. Ma (ORCID: 0000-0002-3191-8952) malimei@bipt.edu.cn, H. Wu (ORCID: 0009-0008-8456-9830) 21121251@bjtu.edu.cn, H. Shen (ORCID: 0000-0003-3341-2805) shenhk@bjtu.edu.cn, T. Wang (ORCID: 0000-0002-7256-883X) wty19850925@mail.tsinghua.edu.cn,

However, these approaches often encounter challenges such as data imbalance, limited generalization across different operating conditions, and the difficulty of capturing essential fault-related characteristics in raw signals. To mitigate these issues, researchers have explored generative models, such as Generative Adversarial Networks (GANs) and diffusion models, to augment fault datasets and improve the robustness of deep learning models [12]. Additionally, feature enhancement techniques, including attention mechanisms and domain adaptation strategies, have been introduced to improve the discriminative power of learned representations, thereby enhancing the performance of unsupervised fault diagnosis methods [13,14]. Despite these advancements, the effectiveness of data-driven methods heavily relies on the quality of input features, underscoring the importance of accurate time-frequency representations (TFR) in fault diagnosis.

Time-frequency analysis (TFA) methods are essential for processing raw vibration signals. They transform non-stationary signals into meaningful TFRs, providing crucial features for machine learning-based fault diagnosis. By providing detailed representations of signal characteristics in both time and frequency domains, TFA enhances feature extraction and contributes to the overall accuracy of data-driven approaches. Consequently, TFA techniques have become indispensable tools for analyzing non-stationary, time-dependent signals, particularly in reliable machinery monitoring systems [15,16]. The essence of TFA lies in refining spectral precision and improving the interpretability of TFRs, which are directly related to the reliability of fault diagnosis. Existing TFA methods can be broadly classified into two categories: one focuses on adjusting the basis functions to better match the frequency variations of the signal, while the other aims to improve the readability of the TFR, which in turn enhances the reliability of fault detection in complex systems.

The classical methods of the first category of TFA include Short-Time Fourier Transform (STFT) [17], Continuous Wavelet Transform (CWT) [18], and Wigner-Ville Distribution (WVD) [19]. To varying extents, these approaches are constrained by the Heisenberg uncertainty principle and affected by cross-term interference, which hinders the acquisition of a clear TFR. These limitations can undermine the reliability of system condition monitoring. Inspired by STFT, researchers modulate the orthogonal basis using modulation terms, allowing the basis to rotate and aligning the frequency-modulated basis with the tangents of the signal's instantaneous frequency (IF) ridge. Based on this concept, the Chirplet Transform (CT) [20] was proposed. This approach is well-suited for handling signals that exhibit linear frequency modulation characteristics but cannot handle nonlinear IF issues or multi-component signals. However, these limitations undermine the reliability of machinery fault diagnosis in complex real-world environments. To accommodate the multi-component IF conditions in practical operating conditions, researchers have proposed numerous improvements, including General Linear Chirplet Transform (GLCT) [21], Velocity-Synchronized Linear Chirplet Transform (VSLCT) [22], Scaled Basis Chirplet Transform (SBCT) [23], self-tuning CT (STCT) [24], Slope-Synchronized Chirplet Transform (SSCT) [25], and Proportional Extraction Chirplet Transform (PECT) [26], among others. While these methods improve TF resolution and energy concentration to varying extents and can identify multi-component IF issues, they are typically based on the assumption that all frequency components are synchronous or proportional. Therefore, they still have significant limitations when analyzing non-proportional IF components composed of different fundamental frequencies. For example, both SBCT and CMCT attempt to match nonlinear IF trajectories by introducing polynomial and frequency-dependent kernel functions to enhance TF energy concentration. However, these methods assume that the IF of signal components are proportional to each other. Consequently, for multi-component signals containing multiple fundamental frequencies, the kernel functions of these two approaches fail to align with all components simultaneously, resulting in TF energy dispersion and blurring artifacts.

The second category of TFA techniques emphasizes enhancing the clarity and interpretability of TFRs, such as the reassignment (RM) [27] method proposed by Auger et al., Generalized reassigning transform [28] method and the Synchronized Synchrosqueezed Transform (SST) [29], the Synchronized Extraction Transform (SET) [30], the Reassignment and Synchrosqueezing [31], and their various improvements. These methods generally focus on energy redistribution to concentrate the TF energy of the main signal, thereby improving the readability of the TFR and enhancing the reliability of machinery fault diagnosis. Additionally, they utilize ridge extraction and optimization to accurately estimate the IF by tracking the TF ridges of the signal. Undoubtedly, TF post-processing techniques partially compensate for the limitations of the original TFR. Nonetheless, their effectiveness is significantly influenced by the quality of the initial TFR and the appropriateness of the parameter configurations. Therefore, if the original TFA fails to accurately analyze the IF trajectories of non-proportional components, the post-processing methods will not be able to extract the correct IF trajectories either.

Both of the above-mentioned categories of TFA methods are unable to address the issue of closely spaced and non-proportional IF. To address this problem, the following conditions must be met: 1) the ability to process multi-component signals with closely spaced instantaneous frequencies; 2) the ability to match different fundamental frequency variations at the same time center. Some researchers have already explored solutions to the non-proportional IF problem. He et al. proposed the Entropy Matching Chirplet Transform (EMCT) [32], which is based on the basis functions of the GLCT. This method filters the region entropy values to obtain a TFR. EMCT can describe the vibration signals of multiple components that are not proportional to each other. For rotating mechanical equipment under complex working conditions, it is easy to have a small frequency interval between the IF ridges. At this time, EMCT cannot handle it well. Wu et al. proposed the General Chirplet Basis Transform (GCBT) [33], which, using the principle of local maxima search at the same time center, identifies multiple chirplet basis function parameters and selects those that match the fundamental frequencies. This approach is capable of handling non-stationary signals that contain multiple non-proportional fundamental frequencies along with their harmonics. However, selecting multiple local maxima at the same time center can easily result in overlapping components between the signal components, which may, to some extent, affect the readability of the TFR.

In summary, to handle non-stationary signals with multiple closely spaced non-proportional fundamental frequencies, this paper develops a novel TFA tool, the Local Entropy Selection Scaling-extracting Chirplet Transform (LESSECT). The main contributions are as follows: First, by analyzing the limitations of SBCT, utilizing Chirp Rate (CR) to form an alternative sub-TFR, and applying entropy optimization, multiple CRs are selected at the same time center to match each non-proportional fundamental frequency. The IF ridges are then re-extracted based on the generated TFR. Compared with other TFA methods, the TFR produced by LESSECT shows more focused TF energy and improves both TF resolution and system reliability. Furthermore, LESSECT effectively addresses the challenges associated with closely spaced and non-proportional IFs, facilitating the analysis of signals containing multiple complex frequency components. This precision in state estimation directly enhances the accuracy of fault detection, thereby playing a key role in improving the overall reliability and performance of the system.

The organization of this paper is outlined as follows: Section 2 discusses the principles and constraints of SBCT, while Section 3 describes the proposed method. In Section 4, the advantages and performance of the proposed method are validated through a series of simulated signals. Section 5 provides verification of the proposed method using three sets of non-proportional experimental signals. Finally, Section 6 summarizes the conclusions of this paper.

2. Theoretical Basis and Research Motivation

2.1. SBCT and Its Limitations

Due to the limitations of CT in analyzing non-stationary, multi-component, and nonlinear signals, Li et al. proposed the SBCT method as an enhancement of CT, which introduces multidimensional parameters and dynamic adjustment mechanisms, enabling the basis functions to dynamically align with the IF trajectories of various signal components. Simultaneously, the improved kernel phase function in SBCT can dynamically adjust the CR based on the signal's time and frequency centers, thus overcoming the limitations of CT and enhancing the accuracy and flexibility of TFA. The key improvements of SBCT are summarized as follows.

To enhance the adaptability of the TF basis, SBCT introduces the time center offset Δu, allowing dynamic adjustment of the window function. By analyzing the rotation angle of the TF basis over the interval $t_c + \Delta u$, SBCT aligns the basis function more effectively with the IF trajectory, thereby improving TF resolution.

$$-tan(\theta) = \sum_{k=1}^{m} k \cdot f_{ok} a_k \cdot (k+1)(u - t_o - \Delta u)^{k-1} \quad (1)$$

In Equation (1), k=1, 2, …, K represents different frequency components, and f_o and t_o represent the time center and frequency centers, respectively. Where θ denotes the rotation angle of the TF basis at the time center t_o, which varies with the frequency center f_o. In other words, the CR is not constant like in CT. Instead, the angle of rotation for the TF basis varies as a function of Δu. When Δu shifts from -L/2 to L/2, the angle of rotation for the TF basis matches with the slope of the IF trajectory within the window. Furthermore, by appropriately selecting the values of a_1, a_2, …, a_m, the CR can closely mimic the slope of the IF trajectory, thereby achieving a better match with the characteristics of the signal.

SBCT is particularly effective when dealing with signals whose IF exhibits a proportional or synchronized relationship, ensuring the accuracy of parameter estimation. It is important to note that the specific values of parameters a_1, a_2, …, a_m can only be determined when the IFs of the target signal are proportional to each other:

$$\frac{\varphi_s''(f_{ov1}, u, t_o)}{\varphi_s''(f_{ov2}, u, t_o)} = \frac{f_{ov1} \sum_{k=1}^{m} k \cdot a_k \cdot (k+1)(u-t_o)^{k-1}}{f_{ov2} \sum_{k=1}^{m} k \cdot a_k \cdot (k+1)(u-t_o)^{k-1}} \quad (2)$$

where f_{ov1} and f_{ov2} denote the central frequencies of two IFs of the target signal at the time center t_o, providing a basis for determining the values of a_1, a_2, …, a_m.

However, this assumption confines SBCT to signals where all frequency components exhibit a proportional or synchronized relationship, limiting its applicability in many real-world scenarios. For example, in industrial equipment, different driving components, such as pumps, compressors, or gearboxes, may operate at different rotational speeds, leading to non-proportional frequency components. Such non-proportional signals can be represented as:

$$z(t) = \sum_{k=1}^{N} z_k(t) = \sum_{k=1}^{N} \sum_{k=1}^{p_k} A_{ki}(t) \exp(-j2\pi \int v_{ki} f_k(t)dt) + \sigma(t) \quad (3)$$

where the signal $z(t)$ consists of multiple fundamental frequency families $z_k(t)$, each containing its harmonics. The harmonic frequencies are determined by the nonstationary fundamental frequency $f_k(t)$ and the multipliers v_{ki} corresponding to each harmonic. N denotes the total count of fundamental frequency families, and p_k represents the number of harmonic components within the k-th family. $A_{ki}(t)$ is the instantaneous amplitude (IA) of the i-th harmonic in the k-th family, varying over time. The phase of each harmonic is given by exp($-j2\pi\int v_{ki} f_k(t)dt$), where v_{ki} scales the harmonic frequency relative to $f_k(t)$ and $\int v_{ki} f_k(t)dt$ represents the accumulated phase. The noise term $\sigma(t)$ accounts for the random component with an amplitude σ. Finally, $Z_k(t)$ denotes the contribution of the k-th family and its harmonics to the overall signal $Z_k(t)$.

From a signal with non-proportional frequency components, selecting any two fundamental frequency components f_1 and f_2, and denoting their time derivatives as f_1' and f_2', the subsequent relationship can be derived:

$$\frac{f_i}{f_i'} \neq \frac{f_j}{f_j'}, i, j \in [1, N], and\ i \neq j \quad (4)$$

From Eq. (2) and Eq. (4), it can be concluded that the SBCT method has significant limitations in handling non-proportional signals. Its core assumption relies on all frequency components in the signal having a clear proportional relationship and synchronization. However, in non-proportional signals, the IF trajectories of the fundamental components vary independently, which violates the theoretical assumptions of SBCT. This results in failure in parameter estimation and decrease in the matching accuracy of the basis functions. Consequently, SBCT cannot effectively process non-proportional signals, requiring more advanced methods to address these issues.

To further illustrate the impact of non-proportional components on SBCT’s performance, we designed controlled numerical experiments to compare its effectiveness on both proportional and non-proportional signals.

First, we construct a set of proportionally simulated signals, as follows:

$$x_{prop}(t) = \sum_{i=1}^{6} sin\left(2\pi \int_0^t v_i(u)du\right) \quad (5)$$

where $v_i(u)$ represents the base frequency for each component i. The term $\int v_i(u)$du represents the cumulative integral of each base frequency signal $v_i(u)$ over time from 0 to t, reflecting the time evolution of the base frequency. The factor 2π scales the result before applying the sine function. The summation of these sinusoidal functions, each corresponding to a different base frequency, results in the simulated signal $x_{prop}(t)$.

$$v_1(u) = \frac{1}{5000} \cdot (u - 30)^2 + 0.5 \quad (6)$$

where $V_2(u)$, $V_3(u)$, $V_4(u)$, $V_5(u)$, and $V_6(u)$ are 0.25, 2.5, 4, 5.2, and 7.1 times the value of $V_1(u)$, respectively. The waveform and IFs are illustrated in Figures 1(a) and 1(b), Using a similar approach, generate a series of non-proportional synthesized waveforms:

$$x_{non-prop}(t) = \sum_{j=1}^{6} a_j \cdot sin\left(2\pi \int_0^t v_j(u)du + \varphi_j\right) \quad (7)$$

where $v_j(u)$ represents the time-dependent frequency for the j-th component, governing the oscillation and time variation of the j-th signal's frequency:

$$\begin{cases} v_1(u) = \frac{1}{300} \cdot (u-30)^2 + 5 \\ v_2(u) = 0.8 \cdot v_1(u) + 0.3 \\ v_3(u) = 1.5 \cdot v_1(u) + 0.2 \\ v_4(u) = -\frac{1}{500} \cdot (u-25)^2 + 3 \\ v_5(u) = 2.1 \cdot v_4(u) + 0.4 \\ v_6(u) = 1.1 v_4(u) + 0.5 \end{cases} \quad (8)$$

Amplitude a_1, a_2, a_3, a_4, a_5, and a_6 are 2.0, 0.8, 1.2, 2, 1.1, and 3; phase φ_1, φ_2, φ_3, φ_4, φ_5 and φ_6, are 0, $\pi/6$, $\pi/4$, $2\pi/3$, $\pi/2$, and $\pi/3$, respectively. the waveform and IFs are depicted in Figures 1(c) and1(d), respectively, with a sampling frequency of 20 Hz.

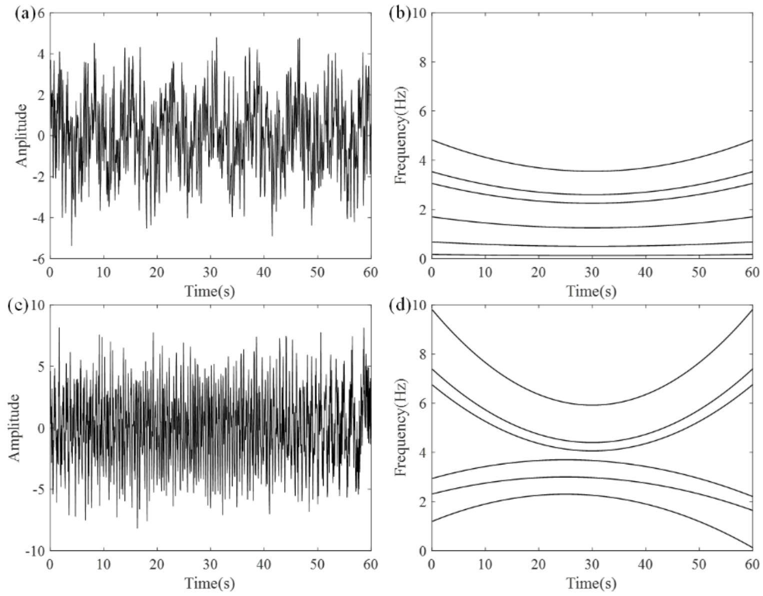

Figure 1. proportional multi-component signal xprop(t): (a) waveform, (b) IFs; non-proportional multi-component signal xnon-prop(t): (c) waveform, (d) Ifs.

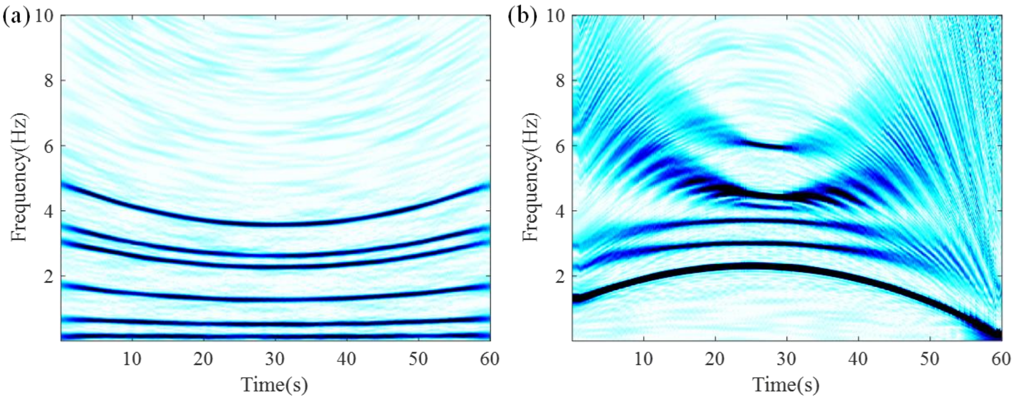

Figure 2. SBCT: (a) TFRs of proportional signal and (b) TFRs of non-proportional signal.

The TFRs obtained by using SBCT to analyse both proportional and non-proportional signals are shown in Figures 2(a) and 2 (b). The TFR corresponding to the proportional signal exhibits concentrated energy and clear trajectories, while the TFR derived from the non-proportional signal shows a dispersed energy distribution and blurred trajectory boundaries, making it difficult to accurately distinguish different components. This demonstrates that SBCT is not suitable for handling non-proportional signals.

2.2. Motivation

Therefore, based on the previous analysis, it is crucial to develop an innovative TFA approach that addresses the challenges posed by signals with non-proportional frequency components. To tackle this issue, the proposed method focuses on handling the complex frequency variations and overlapping component trajectories of non-proportional signals. It integrates dynamic filtering with local optimization to isolate key frequency components, based on the signal's local characteristics. Additionally, the analysis window is dynamically adjusted according to energy distribution properties to optimize the matching of IF trajectories. To further improve accuracy, a multi-level block-by-block analysis and global integration technique is employed. This strategy effectively mitigates issues related to frequency overlap and energy dispersion in complex signals, resulting in significant improvements in energy concentration and the clarity of the TFR.

2.3. CR Matching for Non-Proportional Signals

This section presents the core concept of our proposed method, which involves optimizing multiple CRs at the same time center using Rényi entropy to match different frequency components. The proper selection of CRs is crucial for constructing an adaptive window function, as it directly affects the energy concentration and resolution of the TFR. To ensure that the selected CRs accurately capture the modulation characteristics of the signal, we employ a discretized CR estimation strategy. Specifically, a set of predefined discrete CRs is used to approximate the instantaneous modulation parameters of the signal, and the optimal CR is chosen to enhance energy concentration in the TFR. The mathematical formulation for determining the discrete CRs is presented is as follows.

$$C = tan(\theta) \cdot \frac{F_S}{2T_S} \tag{9}$$

In this equation, C represents the discrete chirp rate, while θ is the rotation angle parameter that determines the orientation and rate of rotation of the TF basis function. The term T_s denotes the sampling period, where F_s is the sampling frequency, which dictates the time resolution in the discrete domain. The function $\tan(\theta)$ controls the tilt of the TF basis function, influencing the adaptability of the transformation to the signal’s varying frequency components.

$$\theta = -\frac{\pi}{2} + \frac{\pi}{N_c+1}, -\frac{\pi}{2} + \frac{2\pi}{N_c+1}, \ \dots, \ \ -\frac{\pi}{2} + \frac{N_c\pi}{N_c+1} \tag{10}$$

Equation (10) defines the discrete set of rotation angles used to determine the corresponding CRs. Here, θ represents the set of discrete angle values associated with different predefined chirp rates. The parameter N_c controls the total number of discrete chirp rate levels, ensuring adequate coverage of possible modulation variations in the signal. While the term $-2\pi/(N_c+1)$ represents the discretization step size of the angle, ensuring an even distribution of the CR candidates.

By using this predefined set of discrete angles, the method can effectively approximate the optimal chirp rate for different signal components, enhancing the accuracy of TFR.

In this context, the optimal CR for the windowed signal is determined by minimizing the Rényi entropy. This ensures that the selected CR aligns precisely with the IF of the windowed signal, thereby enhancing energy concentration in the time-frequency domain (TFD). The underlying principle can be rigorously derived, as demonstrated in the following equation.

$$H^\alpha = \frac{1}{1-\alpha} log_2 \left(\int_{-\infty}^{+\infty} \int_{-\infty}^{+\infty} \left(\frac{\hat{S}(t,\mu)}{\int_{-\infty}^{+\infty} \int_{-\infty}^{+\infty} \hat{S}(t,\mu) dt d\mu} \right)^\alpha dt d\mu \right) \tag{11}$$

Here, H^α represents the entropy of the TFR. Here, H^α represents the entropy of the TFR, where α is typically set to 3. It is minimized when the CR matches the IF of the signal, leading to better energy concentration in the TFR. The entropy expression generalizes the energy distribution across time and frequency. The integral over $S(t, \mu)$, the signal's TFR, represents the energy spread across frequency bands. Lower entropy indicates energy concentration in specific regions, which occurs when the CR aligns with the signal's frequency components.

$$\begin{aligned} H(c) &= \frac{1}{1-\alpha} log_2 \left(\int_{-\infty}^{+\infty} \int_{-\infty}^{+\infty} \left(\frac{e^{-\hat{\sigma}^2(\mu-\phi'(t))^2}}{\int_{-\infty}^{+\infty} \int_{-\infty}^{+\infty} e^{-\hat{\sigma}^2(\mu-\phi'(t))^2} dt d\mu} \right)^\alpha dt d\mu \right) \\ &= \frac{1}{1-\alpha} log_2 \left(\int_{-\infty}^{+\infty} \int_{-\infty}^{+\infty} \left(\frac{e^{-(\hat{\sigma}\mu-\hat{\sigma}\phi'(t))^2}}{\int_{-\infty}^{+\infty} \int_{-\infty}^{+\infty} e^{-(\hat{\sigma}\mu-\hat{\sigma}\phi'(t))^2} dt d\mu} \right)^\alpha dt d\mu \right) \\ &= H(c)|_{\sigma=1} - log_2(\hat{\sigma}) \end{aligned} \tag{12}$$

From Equation (12), we observe that H^α decreases as the CR increases. The optimal CR corresponds to the point where it aligns perfectly with the IF, minimizing entropy and ensuring a concentrated TFR.

By minimizing H^{α}, we select the CR that best matches the signal's modulation, resulting in optimal energy concentration in the TFR and an accurate representation of the TF structure. This confirms that the optimal CR minimizes the Rényi entropy and aligns with the signal's IF.

Due to the significant modulation differences in both time and frequency domains in multi-component signals, it is essential to design a method that can effectively adapt to these differences. The key challenge lies in dynamically adjusting the CR according to the varying frequency components of the signal to achieve adaptive TFA. By observing the signal's characteristics in small time and frequency intervals, we find that the signal can be approximated as a linear frequency modulation signal in certain local regions, providing an effective approximation for TFA.

Based on this observation, this study proposes a method of partitioning the entire TF plane into several TF blocks. By calculating the Rényi entropy for each TF block separately, we can quantify the energy distribution of the signal in each local region and optimize the analysis results. Specifically, a sliding window approach is used to partition the TFR $S(t, \mu)$ along the time and frequency axes, ensuring full coverage of the entire TF plane. The signal characteristics within each window influence the final TFR, helping to optimize the overall signal analysis.

The partitioning of the TF plane and the Rényi entropy calculation process can be mathematically described by equations (13) and (14). This approach not only improves the accuracy of TFA but also better captures the changes and modulation characteristics of the frequency components in the signal, ultimately optimizing the overall signal processing performance.

$$R(c,t,\mu) = \frac{1}{1-\alpha} log_2 \left(\int_{-\infty}^{+\infty} \int_{-\infty}^{+\infty} \frac{|S(c,\zeta,\gamma) M(\zeta-t,\gamma-\mu)|}{\int_{-\infty}^{+\infty} \int_{-\infty}^{+\infty} |S(c,\zeta,\gamma)| M(\zeta-t,\gamma-\mu) d\zeta d\gamma} \right) d\zeta d\gamma \tag{13}$$

In Equation (13), $R(c,t,\mu)$ represents the Rényi entropy of the TFR of a signal at a specific CR c, time t, and frequency μ. Here, α is the Rényi entropy order, determining the degree of concentration in the entropy calculation. The term $S(c,\zeta,\gamma)$ represents the TFR of the signal at chirp rate c and frequency variables ζ and γ, while $M(\zeta-t, \gamma-\mu)$ is the windowing function used to partition the TFR.

$$M(t,\mu) = \begin{cases} 1, & -\frac{\Delta t}{2} < t < \frac{\Delta t}{2}, \quad -\frac{\Delta \mu}{2} < t < \frac{\Delta \mu}{2} \\ 0, & otherwise \end{cases} \tag{14}$$

In Equation (14), $M(t,\mu)$ is a binary window function that defines the TF region over which the entropy calculation is applied. It has a value of 1 within the window defined by the time and frequency intervals Δt and $\Delta \mu$, respectively, and 0 outside this region. Δt and $\Delta \mu$ represent the time and frequency sizes of the TF block, respectively.

To better capture the TF characteristics of the signal, we introduce a new variable N_c and map the signal from the time domain to a three-dimensional TF space $S(c,t,\mu)$ with dimensions $N_c \times L \times L/2$. In this process, different CRs applied to SBCT yield a set of distinct TFRs. To improve the accuracy of the TFRs, we divide the signal's TFD into several TF blocks, specifically $M_t \times M_\mu$ blocks. The Rényi entropy of each block is used to quantify the distribution of energy within that block.

By applying Equation (13), we can calculate the Rényi entropy for each TF block, resulting in a new three-dimensional TF space $S(c,t,\mu)$, where the dimensionality is reduced from the original high-dimensional space to $N_c \times M_t \times M_\mu$. The Rényi entropy value of each block reflects the degree of energy concentration in both the time and frequency directions. The block with the lowest entropy is selected as the ideal TF block, indicating that its CR has achieved the best match with its corresponding TF characteristics. This can be expressed as:

$$\hat{c}(t,\mu) = \underset{c}{argmin}\{R(c,t,\mu)\} \tag{15}$$

Through the above approach, we combine these selected blocks to construct a two-dimensional TFR with dimensions $L \times L/2$, exhibiting higher energy concentration and significantly enhancing the overall clarity of the TFR.

By utilizing the two-dimensional Rényi entropy-based calculation method, we effectively enhance the TF resolution of the TFR, enabling it to more accurately reflect the TF characteristics of the signal. This method improves the quality of the TFR by optimizing the selection of CRs and energy distribution. The resulting enhanced TFR better aligns with the signal's frequency modulation characteristics, further improving the signal's interpretability. The TFR of the SBCT selected through entropy can be defined as the entropy- SBCT (ESBCT).

3. Local Entropy Selection Scaling-extracting Chirplet Transform

This section focuses on improving the TF resolution of LESSECT to achieve a more refined TFR. To lay the groundwork for this enhancement, we first provide a brief overview of the original SET method. The core logic of SET is based on STFT, where only the energy related to the IF trajectory of the signal is retained, while the blurred parts of the distribution are discarded. This results in a TFR with enhanced energy focus. The TFR of a non-stationary signal obtained through STFT is given by:

$$\begin{cases} F(t,\mu) = \int_{-\infty}^{\infty} g(\varphi - t) \cdot s(\varphi) \cdot e^{-jw(\varphi - t)} d\varphi \\ s(t) = A_{(t)} \cdot e^{j\theta(t)} \end{cases} \tag{16}$$

where $g(\varphi\text{-}t)$ is the window function, and $s(t)$ denotes the non-stationary signal, $A_{(t)}$ corresponding to the IA and $\theta(t)$ corresponding to the Instantaneous phase (IP), respectively. With parseval's theorem, an additional phase shift $e^{j\xi t}$ as:

$$F(t,\mu) = (1/2\pi) \int_{-\infty}^{\infty} \hat{g}(\mu - \varphi) \cdot \hat{s}(\varphi) \cdot e^{j\xi t} d\varphi \tag{17}$$

we employ the model of a purely harmonic signal，the STFT given in Eq. (19) can be elaborated as:

$$F(t,\mu) = A \cdot \hat{g}(\mu - \mu_0) \cdot e^{j\omega_0 t} \tag{18}$$

where A denotes the fixed amplitude and μ_0 represents constant frequency.

The SET can only capture the TF points along the IF trajectory $\mu_0(t,\mu)$，The IF is calculated by taking the time derivative of $F(t, \mu)$.

$$\frac{\partial F(t,\mu)}{\partial t} = \int s(\varphi) \cdot \frac{g(\varphi - t)}{\partial \varphi} \cdot e^{-j\mu\varphi} d\varphi = F(t,\mu) \cdot i\mu_0 \tag{19}$$

With Eq. (22), the IF trajectory $\mu_0(t, \mu)$ is structured as:

$$\omega_0(t,\mu) = -i \cdot \left[\frac{\frac{\partial F(t,\mu)}{\partial t}}{F(t,\mu)} \right] \tag{20}$$

From Eq. (23). if $F(t, \mu)$ is not zero, the IF associated with the STFT coefficients must always correspond to $\mu_0(t, \mu)$. The Dirac expression of the SEO is given below:

$$\delta(\mu - \mu_0(t,\mu)) = \begin{cases} 1, \mu = \mu_0(t,\mu) \\ 0, \mu \neq \mu_0(t,\mu) \end{cases} \tag{21}$$

To avoid errors in the estimation of IFs and attain more precise computation of the temporal derivative of the STFT $\partial_t F(t, \mu)$ the following formula is provided:

$$\frac{\partial F(t,\mu)}{\partial t} = j\mu \cdot F(t,\mu) - F^{(g)}(t,\mu) \tag{22}$$

where $F^{(g)}(t,\mu)$ represents the derivative of the window function. By utilizing Eq. (23) and Eq. (25), a more precise estimation of the IF can be derived as:

$$\mu_0(t,\mu) = \mu + i \cdot \frac{F^{(g)'}(t,\mu)}{F(t,\mu)} \tag{23}$$

where $(g)'$ represents the derivative of the window function. By substituting Eq. (26) into Eq. (24), the SEO is revised as:

$$\delta(\mu - \mu_0(t,\mu)) = \begin{cases} 1, -i \cdot \left(\frac{F^{(g)'}(t,\mu)}{F(t,\mu)} \right) = 0 \\ 0, -i \cdot \left(\frac{F^{(g)'}(t,\mu)}{F(t,\mu)} \right) \neq 0 \end{cases} \tag{24}$$

employs the real component of the SEO, represented as:

$$\delta(\mu - \mu_0(t,\mu)) = \begin{cases} 1, \left| Re\left(i \cdot \frac{F^{(g)'}(t,\mu)}{F(t,\mu)} \right) \right| < \delta \\ 0, \left| Re\left(i \cdot \frac{F^{(g)'}(t,\mu)}{F(t,\mu)} \right) \right| \geq \delta \end{cases} \tag{25}$$

Delta represents the discrete frequency interval, which needs to be appropriately selected. An excessively small delta may result in the loss of some time-varying TF points. After dynamic adjustment, the SET is defined as:

$$F(t,\mu) = F(t,\mu) \cdot \delta(\mu - \mu_0) \tag{26}$$

3.1. The Proposed LESSECT method

As known from Section 2.1, the final TFR of the SBCT is:

$$SBCT_s(t,\mu) = \int_{-\infty}^{+\infty} s(\varphi) \mu_\sigma(\varphi - t_o) e^{-j\mu(\varphi - t)} d\varphi \tag{27}$$

As previously discussed in Section 2.3, the introduction of the two-dimensional Rényi entropy-based calculation effectively enhances the TF resolution by optimizing the selection of CRs and refining energy distribution. Building on this foundation, ESBCT is formulated to achieve better energy concentration in the TFR. Based on this, we further develop the LESSECT method.

Referring to Eq. (21), Eq. (33) is further expressed as:

$$ESBCT_s(t,\mu) = A \cdot \hat{g}(\mu - \hat{\mu}_0) \cdot e^{j\hat{\mu}_0 t} \tag{28}$$

Further integrates into the form of Eq. (22).

$$\frac{\partial F(t,\mu)}{\partial t} = ESBCT_s(t,\mu) \cdot i\hat{\mu}_0 = A \cdot \hat{g}(\mu - \hat{\mu}_0) \cdot e^{j\hat{\mu}_0 t} \cdot i\hat{\mu}_0 \tag{29}$$

Update the IF trajectory $\mu_0(t,\mu)$ of Eq. (23) using Eq. (34).

$$\hat{\omega}_0(t,\mu) = -i \cdot \left(\frac{\frac{\delta F(t,\mu)}{\delta t}}{F(t,\mu)} \right) = -i \cdot \left(\frac{\frac{\delta ESBCT_S(t,\mu)}{\delta t}}{ESBCT_S(t,\mu)} \right) \tag{30}$$

Subsequently, the updated SEO_{SBCT} can be obtained based on the original SEO.

$$\delta_s(\mu - \hat{\mu}_0(t,\mu)) = \begin{cases} 1, \mu = \hat{\mu}_0(t,\mu) \\ 0, \mu \neq \hat{\mu}_0(t,\mu) \end{cases} \tag{31}$$

Referring to Eq. (26), a more accurate IF estimation is expressed as:

$$\hat{\omega}_1(t,\mu) = \mu + i \cdot \left(\frac{\frac{\delta ESBCT^{(g)'}{}_s(t,\mu)}{\delta t}}{ESBCT_S(t,\mu)} \right) \tag{32}$$

Similarly, the SEO_{SBCT} in Eq. (34) can be updated as:

$$\delta_s(\mu - \hat{\mu}_1(t,\mu)) = \begin{cases} 1, -i \cdot \left(\frac{\frac{\delta ESBCT^{(g)'}{}_s(t,\mu)}{\delta t}}{ESBCT_S(t,\mu)} \right) = 0 \\ 0, -i \cdot \left(\frac{\frac{\delta ESBCT^{(g)'}{}_s(t,\mu)}{\delta t}}{ESBCT_S(t,\mu)} \right) \neq 0 \end{cases} \tag{33}$$

The final algorithm implementation relies on the real component of the SEO_{SBCT}, represented as:

$$\delta_s(\mu - \hat{\mu}_1(t,\mu)) = \begin{cases} 1, \left| Re\, i \cdot \left(\frac{\frac{\delta ESBCT^{(g)'}{}_s(t,\mu)}{\delta t}}{ESBCT_S(t,\mu)} \right) \right| < \delta \\ 0, \left| Re\, i \cdot \left(\frac{\frac{\delta ESBCT^{(g)'}{}_s(t,\mu)}{\delta t}}{ESBCT_S(t,\mu)} \right) \right| \geq \delta \end{cases} \tag{34}$$

δ represents the discrete frequency interval used in the LESSECT method. It controls the resolution of the frequency analysis. A smaller delta can result in a higher frequency resolution, helping to capture more detailed features of the TFR. This can lead to a clearer, sharper result, especially when analyzing rapidly changing signals. However, choosing an excessively small delta can cause a loss of some time-varying TF points, particularly for signals with wide-band or rapidly changing characteristics. This is because smaller intervals may fail to capture the necessary information for certain parts of the signal.

Therefore, it's important to strike a balance between a sufficiently small delta for enhanced resolution and a larger delta that preserves the time-varying nature of the signal. In practice, a delta value of 0.5 is often recommended, as it offers a good trade-off between frequency resolution and maintaining the integrity of the TF points. The SET method is then defined based on this chosen delta, dynamically adjusting the TF points while avoiding the loss of crucial signal features.

Finally, according to Eq. (40), the proposed LESSECT can be formulated as:

$$LESSECT(t,\mu) = ESBCT(t,\mu) \cdot \delta_s(\mu - \hat{\mu}_1(t,\mu)) \tag{35}$$

The structure and details of the LESSECT algorithm introduced in this study are summarized within Table 1.

Table 1. LESSECT algorithm.

TFA method: LESSECT
Step 1: Initial parameter assignment
（1） Input signal $x(t)$, window size L, sampling rate Fs, and the number of gaussian window K, Number of divisions for rows and columns in localized entropy optimization. N_{nd}, N_{nc}, the parameters ε and *delta.*
（2） *sub*-TFR←zeros(N_F, N_k).
（3） We obtain a series of discretized angles using the following formula: $$\theta_m = -\frac{\pi}{2} + \frac{m\pi}{M+1}, m \in \{1,2,\ldots,M\}$$
Step 2: Calculate the sub-TFR
for i=1:N_F
for j=1:N_F
sub-TFR(:,:,i,j)←SBCT(t, ω).
sub-TFR^g(:,:,i,j)←$SBCT^{g'}$(t, ω).
end for
end for
Step3: Localized Entropy Selection
（4） Introduce Rényi entropy and partition the sub-TFR blocks.
for c = 1:N
ESBCT(:, :) ← min(renyi(*sub*-TFR (:,:,c)))
$ESBCT^{(g)'}$(:, :) ← min(renyi(*sub*-TFR^g(:,:,c)))
end for
Step 4: Synchroextracting
（5） Calculate:E←*mean*(*abs*($s(t)$)).
for i=1:N_k
for j=1:N_k
if *abs*(ESBCT(i,j))≥ε·E
if *abs*($\boldsymbol{Re}\left(\boldsymbol{i} \cdot \frac{\boldsymbol{ESBCT^{(g)'}(i,j)}}{\boldsymbol{ESBCT(i,j)}}\right)$)<*delta*
$\delta_s(i,j)$=1
end if
end if
end for
end for
（6） LESSET(i,j)←ESBCT(i, j)$\delta_s(i, j)$.
（7） Output: LESSET(t, ω)

4. Numerical simulations

This section presents a simulation study to validate the effectiveness of LESSECT in analyzing non-proportional signals. The performance of LESSECT is assessed in comparison with other TFA techniques, with a primary emphasis on energy concentration, TF resolution, and the adaptability of the TFR. To illustrate this, we consider a complex set of signals, whose specific construction formulas are provided as follows:

$$s_1(t) = \sum_{i=1}^{5} A_i(t) \cdot sin(2\pi \int_0^t f_i(t)\,dt) + \sigma\ (t) \tag{36}$$

To better reflect practical conditions, a synthetic signal is generated with an added 10 dB signal-to-noise ratio (SNR). In particular, the IF trajectories of each component are as follows:

$$\begin{cases} f_1(t) = 71 + 20\,sin(\frac{\pi}{2}t) \\ f_2(t) = 68 + 20\,sin(\frac{\pi}{2}t) \\ f_3(t) = \frac{1}{300}(t-30)^2 + 40 \\ f_4(t) = 5 + 10\,sin(\frac{\pi}{4}t) \\ f_5(t) = 25 + 5\,cos(\frac{2\pi}{5}t) \end{cases} \tag{37}$$

The magnitudes of these components are defined as follows: $A_1(t)$=1.0, $A_2(t)$=1.1, $A_3(t)$=0.8, $A_4(t)$=0.6, $A_5(t)$=0.5. The synthetic signal is then processed using LESSECT. The target signal is sampled at a frequency of f_s=200Hz and analyzed over a duration of t_{tend}=4s. It is constructed by superimposing the individual signal components defined in the aforementioned equations. Finally, the time-domain representation of the noisy target signal $s_1(t)$ is presented. The signal waveform and its corresponding ideal TFR are illustrated in Figure 3(a) and Figure 3(b), respectively.

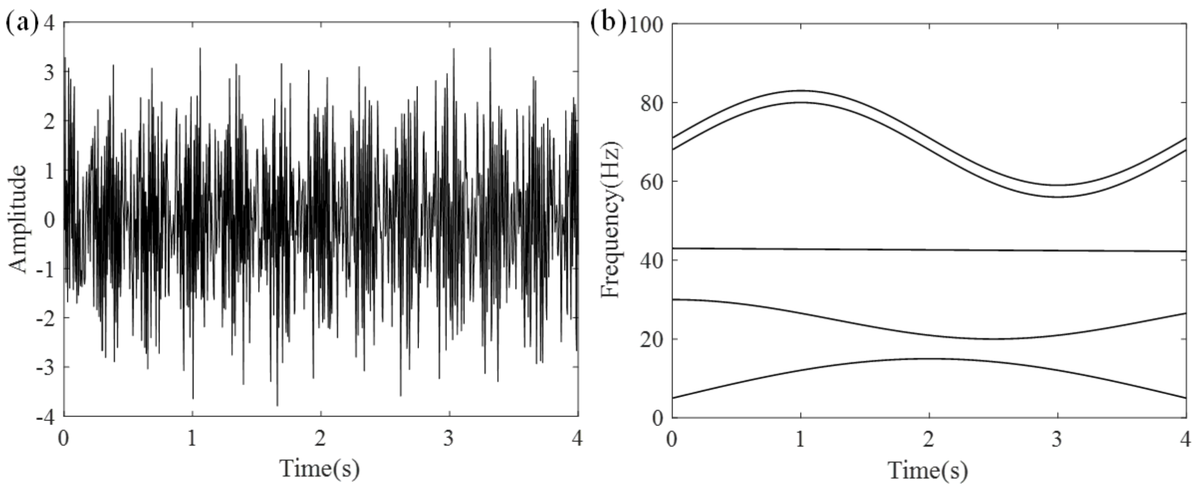

Figure 3. The synthetic signal s1(t): (a) Waveform; (b) Ideal TFR.

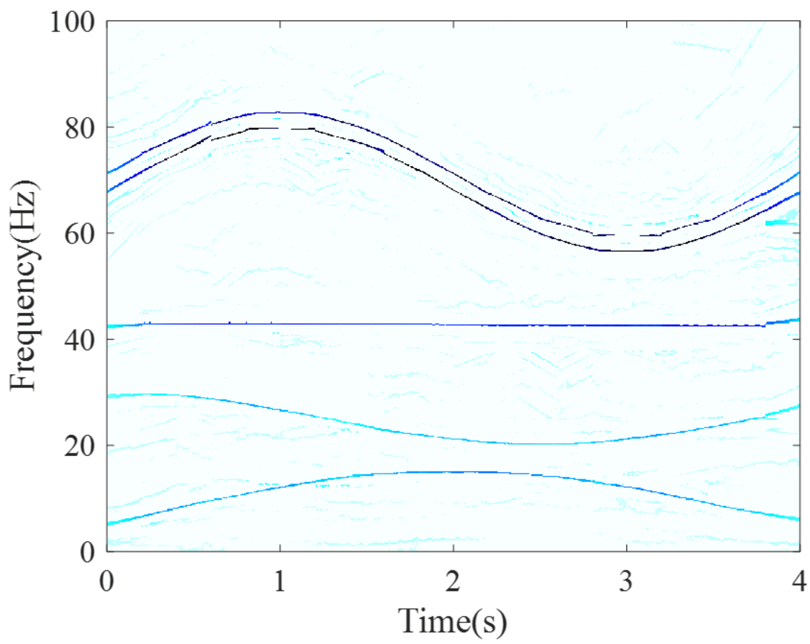

Figure 4. TFR of s1(t) obtained using LESSECT.

The LESSECT approach is applied to the synthetic signal $s_1(t)$ for TFA, with the results shown in Figure 4. LESSECT effectively captures the time-varying characteristics of all IFs, yielding a well-structured TFR with superior TF resolution and energy concentration, demonstrating its enhanced performance in TFA.

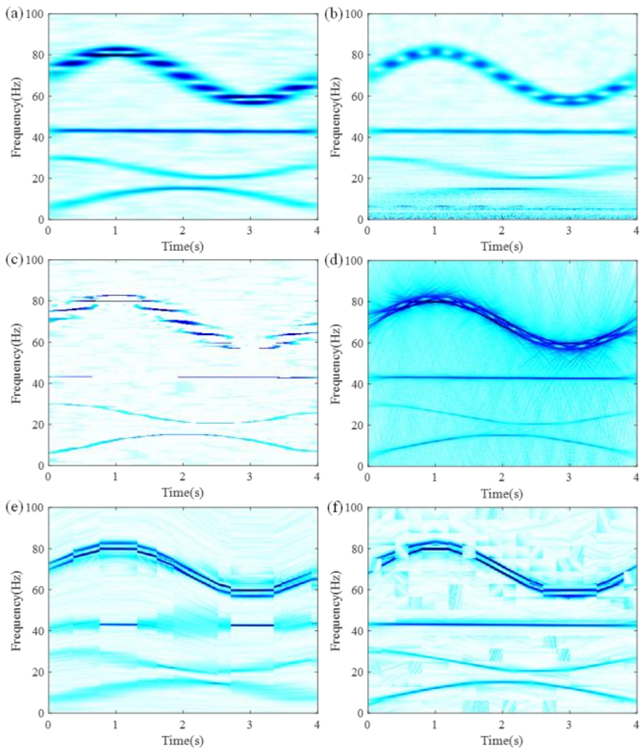

Figure 5. TFR results of s1(t) using different methods: (a) STFT; (b) CWT; (c) SET; (d) GLCT; (e) SBCT; (f) EMCT.

To comprehensively evaluate the effectiveness of the LESSECT method, a comparative analysis was conducted against both traditional and advanced TFA techniques, including STFT, CWT, SET, GLCT, SBCT, and EMCT. The TFRs obtained from these methods are presented in Figure 5. A detailed examination of these results reveals that conventional approaches exhibit noticeable limitations. Specifically, the TFRs generated by these techniques tend to be blurry and lack coherent TFRs. The IF trajectories produced by these methods are often discontinuous, leading to poor interpretability. Additionally, varying degrees of energy leakage can be observed, further degrading the clarity and concentration of the TFRs.

To quantitatively assess the energy concentration of different TFA methods, the Rényi entropy of each TFR was computed, as summarized in Table 2. This metric effectively measures the distribution of energy in the TF plane, where a lower entropy value indicates higher energy concentration. The results demonstrate that LESSECT achieves the lowest Rényi entropy, signifying superior energy localization. In contrast, GLCT exhibits the highest entropy, indicating severe energy dispersion. This suggests that LESSECT provides a more compact and well-defined TFR, mitigating the common issue of energy leakage encountered in conventional methods.

Table 2. Rényi Entropy Comparison of 7 TFA Methods.

method	STFT	CWT	SET	GLCT	SBCT	EMCT	LESSECT
Rényi entropy	16.8664	16.8239	14.6617	18.4628	15.8744	16.7705	13.7877

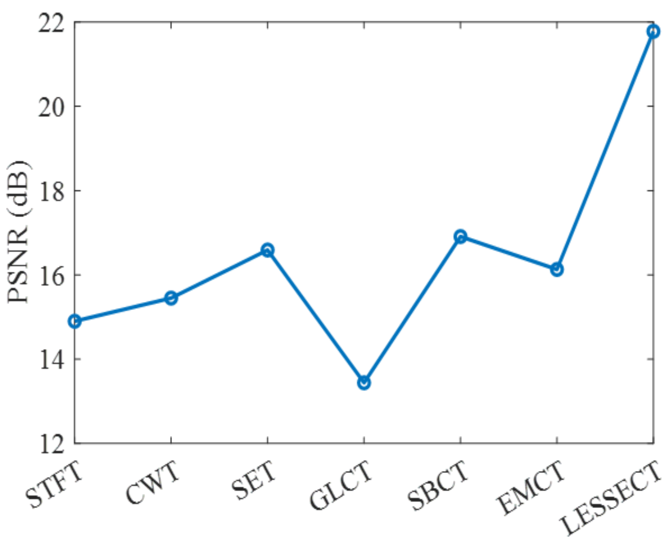

Figure 6. PSNR Comparison of Different TFA Methods.

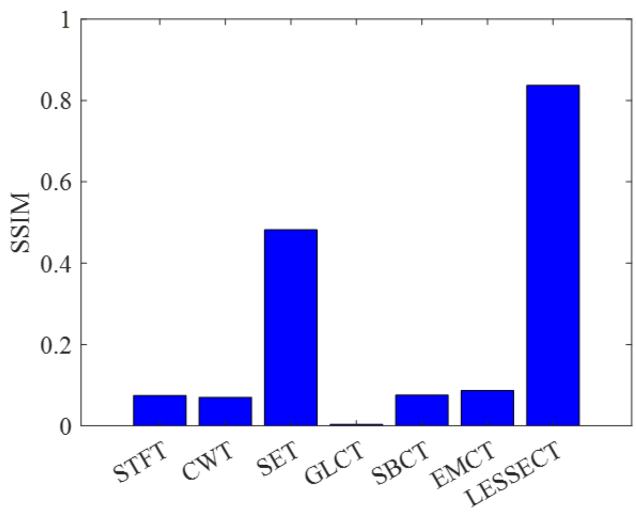

Figure 7. SSIM Comparison of Different TFA Methods.

Beyond energy concentration, additional quantitative measures were introduced to further validate the performance of LESSECT. Specifically, peak signal-to-noise ratio (PSNR) and structural similarity index (SSIM) were employed to evaluate the fidelity and structural integrity of the TFRs, respectively. PSNR quantifies the level of distortion in reconstructed signals, with a higher value indicating better preservation of the original signal characteristics. SSIM, on the other hand, measures the structural similarity between the estimated and reference TFRs, with values approaching 1 signifying high resemblance. Figure 6 presents the PSNR values for different methods, highlighting that LESSECT achieves the highest PSNR. This suggests that LESSECT generates a more accurate and less distorted TFR compared to other approaches. Notably, GLCT exhibits the lowest PSNR, reinforcing its tendency to produce high levels of distortion. Similarly, Figure 7 illustrates the SSIM comparison, where LESSECT attains the highest SSIM value, demonstrating its ability to closely replicate the ideal TFR structure. Conversely, GLCT shows the lowest SSIM, indicating a significant deviation from the expected representation.

In summary, LESSECT consistently outperforms existing TFA techniques across multiple evaluation metrics. With superior energy concentration, minimal distortion, and high structural fidelity, it ensures a more coherent and continuous TFR. Notably, LESSECT excels in capturing intricate TF structures and accurately analyzing non-proportional signals, demonstrating strong adaptability and robustness for complex non-stationary signal processing.

5. Practical verifications

This section evaluates the performance of LESSECT using three sets of experimentally acquired signals. The first dataset consists of bat echolocation signals, the second comprises rolling bearing fault data collected from the Spectra Quest Machinery Fault Simulator (MFS-PK5M), and the third includes vibration signals recorded from a wind turbine planetary gearbox test rig.

5.1. the test of Bats echolocation call

The first experiment focuses on the analysis of bat echolocation calls. Bats emit ultrasonic pulses and rely on a series of high-frequency short pulses for echolocation. When these sound waves encounter objects, they reflect back as echoes. The resulting signals exhibit non-proportional IF characteristics. To validate the effectiveness of LESSECT, the TFR obtained using LESSECT is compared against those produced by STFT, CWT, SET, GLCT, SBCT, and EMCT, demonstrating its ability to accurately capture the TF characteristics of such complex signals.

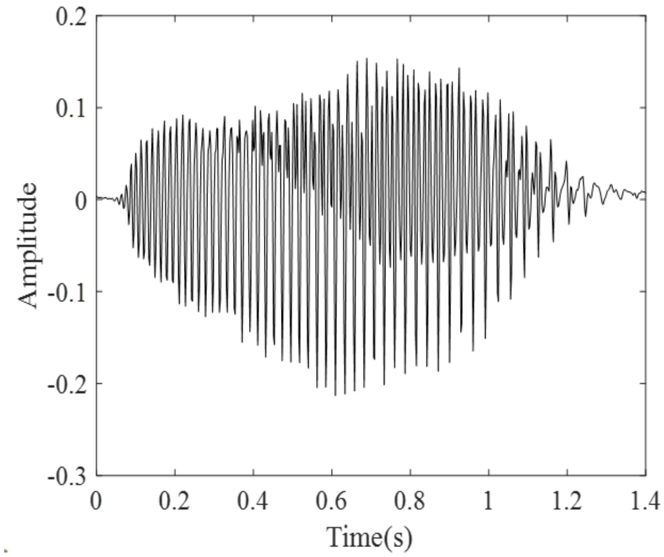

Figure 8. The waveform of Bats echolocation call.

The bat echolocation call is sampled at 450 Hz with a duration of 1.4 s. The vibration signal and the corresponding LESSECT-based TFR are presented in Figures 8 and 9, respectively. The window function length is set to 200. To assess the effectiveness of LESSECT, a comparative analysis is conducted against STFT, CWT, SET, GLCT, SBCT, and EMCT, ensuring consistent parameter settings across all methods.

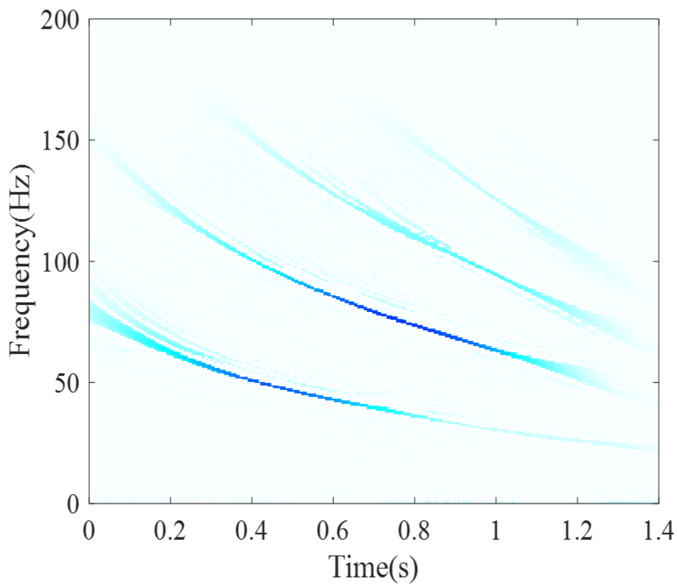

Figure 9. TFR of Bats echolocation call obtained using

LESSECT.

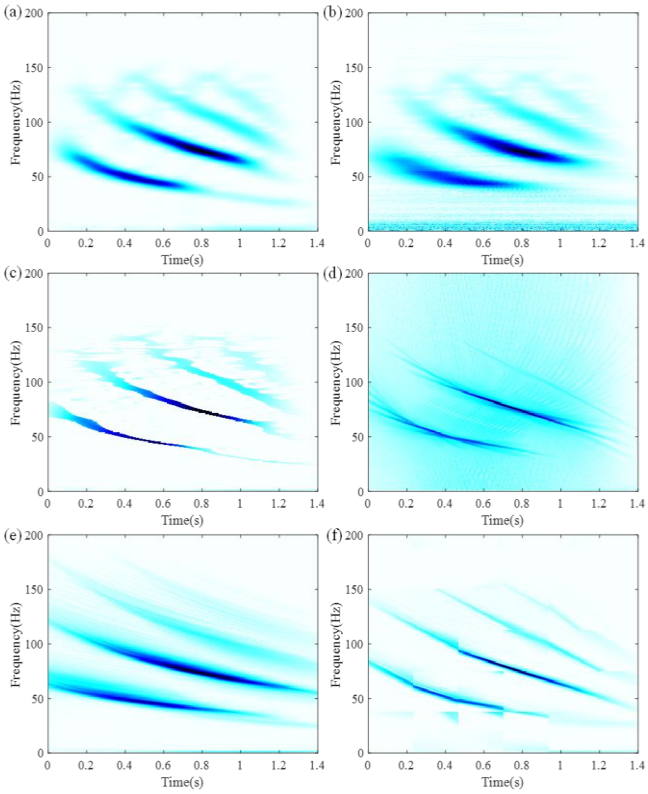

Figure 10. TFR results of Bats echolocation call using different methods: (a) STFT; (b) CWT; (c) SET; (d) GLCT; (e) SBCT; (f) EMCT.

In LESSECT accurately identifies the four frequency components of the bat echolocation signal and demonstrates a high level of energy concentration in the TFR. As shown in Figure 9, LESSECT provides superior TF resolution compared to other methods. In contrast, other TFA methods exhibit various limitations. Figure 10(a)–Figure 10(f) illustrate these shortcomings: GLCT fails to resolve the high-frequency components effectively; the TFR produced by SET lacks clarity; EMCT exhibits energy dispersion in certain TF regions, with non-smooth IF trajectories; and STFT, CWT, and SBCT suffer from varying degrees of energy leakage and blurring effects.

To further quantify the differences in energy concentration among these methods, Table 2 presents the Rényi entropy values for each TFR. A lower Rényi entropy indicates higher energy concentration. As shown in the table, LESSECT achieves the lowest entropy value, suggesting its superior ability to maintain energy focus. In contrast, GLCT has the highest entropy, reflecting severe energy dispersion.

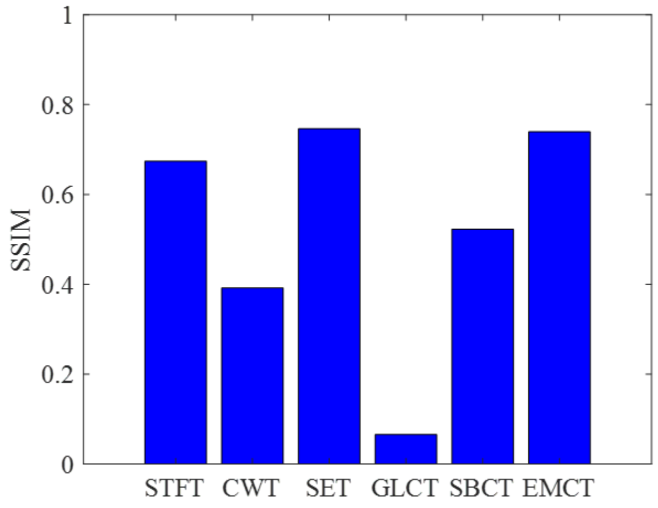

Figure 11. SSIM-Based Evaluation of TFR Methods with LESSECT as the Reference.

Additionally, to assess the structural similarity of different TFRs, the SSIM metric was employed for comparative analysis. Taking the TFR generated by LESSECT as the reference, Figure 11 presents the SSIM values between LESSECT and the other six methods. The results reveal that SET and EMCT achieve relatively high SSIM values, indicating better preservation of TFR structures. Conversely, GLCT yields the lowest SSIM value, signifying a substantial deviation from the LESSECT-generated TFR. Overall, the quantitative results confirm that LESSECT exhibits superior performance in both energy concentration and TFR clarity.

In summary, the IF components of the analyzed signal exhibit a non-proportional frequency structure. Despite this complexity, LESSECT successfully generates a highly concentrated TFR with clear TF energy distribution. Compared to the six other TFA methods, LESSECT effectively mitigates the challenges posed by non-proportional IF components, demonstrating its superior capability in TFR.

5.2. Fault testing of rolling bearing inner race defects

The second set of experiments was conducted on the MFS-PK5M platform to simulate rolling bearing faults, specifically targeting inner race defects [34,35].

Table 3. Rényi Entropy Comparison of 7 TFA Methods.

method	STFT	CWT	SET	GLCT	SBCT	EMCT	LESSECT
Rényi entropy	14.5402	15.7009	13.0020	16.8362	14.1393	13.9399	11.5327

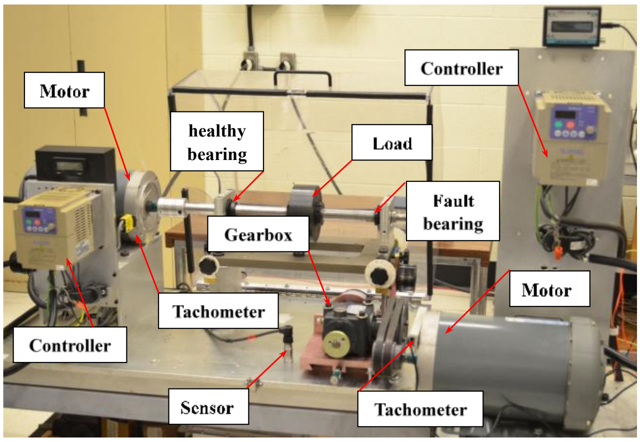

Figure 12. Test Platform for Rolling Bearing Fault Simulation Experiments.

Figure 12 illustrates the test rig, while Table 3 details the specifications of the faulty bearing along with its fault characteristic frequencies (FCFs). In this context, f_r represents the rotational frequency of the bearing. Vibration signals were acquired using accelerometers at a sampling rate of 200 kHz. During the experiment, the bearing's rotational speed ranged from 13 Hz to 25.7 Hz. The faulty bearing vibration signal is downsampled to 600 Hz over a duration of 4 s. Figure 13(a) and Figure 13(b) present the signal and the corresponding time-varying bearing speed curve, respectively. The window function size is set to 450. To evaluate the performance of LESSECT, a comparative analysis is conducted using STFT, CWT, SET, GLCT, SBCT, and EMCT, ensuring consistent parameter settings across all methods.

Table 4. Specifications for the bearings employed in the inner race fault test.

Bearing type	Fault type	Pitch diameter	Number of balls	Ball diameter	FCF
ER16K	inner race fault	38.52mm	9	7.94mm	$5.43f_r$

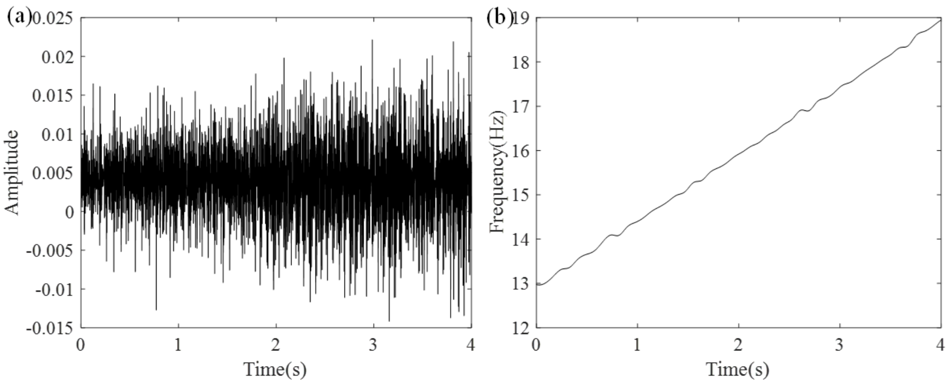

Figure 13. The vibration data from the faulty bearing: (a) Waveform; (b) RF.

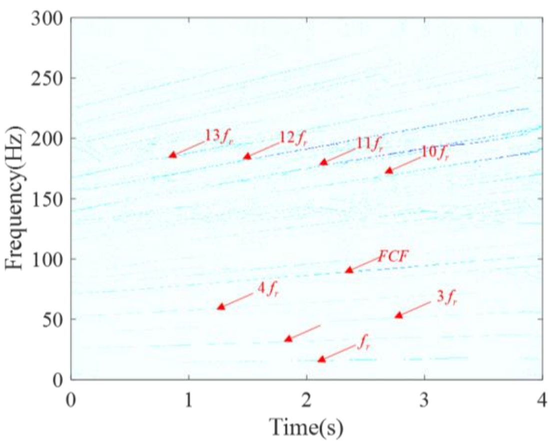

Figure 14. TFR obtained using LESSECT for the faulty bearing vibration signal.

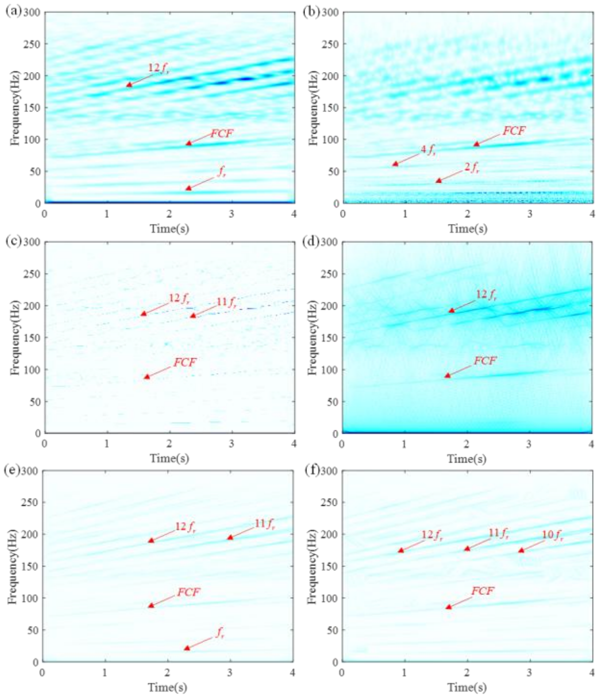

Figure 15. TFR results for the faulty bearing vibration signal using different methods: (a) STFT; (b) CWT; (c) SET; (d) GLCT; (e) SBCT; (f) EMCT.

As shown in Figure 14, LESSECT effectively captures the FCF with high accuracy and the bearing's harmonic frequencies, such as f_r, $2f_r$, $3f_r$, $10f_r$, $11f_r$, $12f_r$, etc., with a high concentration of TF energy. However, among other TFA methods, STFT, CWT, and GLCT exhibit varying degrees of energy leakage and blurring effects, only being able to extract individual low-frequency components, As depicted in Figure 15(a), Figure 15 (b), and Figure 15 (d). The SET method experiences energy disturbance, with intermittent and incomplete IF trajectories, and fails to fully identify relevant turning frequencies, as illustrated in Figure 15(c). In the TFR results calculated using SBCT and EMCT, more accurate observation of bearing FCF and some high-frequency components, such as 10 f_r and 11 f_r, can be seen. However, they are unable to accurately extract low-frequency signal components, showing blurring effects, as shown in Figure 15 (e)–Figure 15 (f).

Table 5. Rényi Entropy Comparison of 7 TFA Methods.

method	STFT	CWT	SET	GLCT	SBCT	EMCT	LESSECT
Rényi entropy	19.3523	18.4348	17.1607	20.7281	18.0346	19.0019	15.7139

Following the previous analysis of TFR results for the faulty bearing vibration signal, we further evaluate the energy concentration of different methods by computing their Rényi entropy, as shown in Table 4. A lower entropy value indicates a higher concentration of TF energy, while a higher entropy value suggests greater energy dispersion and blurring effects. The results demonstrate that LESSECT achieves the lowest Rényi entropy, highlighting its superior ability to maintain energy concentration. In contrast, GLCT exhibits the highest entropy, indicating severe energy diffusion in its TFR. Moreover, STFT, CWT, SBCT, and EMCT also yield relatively high entropy values, reflecting varying degrees of energy leakage and blurring.

To further quantify the differences in TFR quality among the methods, SSIM is computed with the LESSECT-generated TFR serving as the reference for comparison. The SSIM values between LESSECT and the six other methods (STFT, CWT, SET, GLCT, SBCT, and EMCT) are presented in Figure 16. A higher SSIM value indicates greater structural similarity between the compared TFR and the LESSECT baseline, signifying better TFR. The results show that SET achieves the highest SSIM, suggesting that its TFR closely resembles that of LESSECT, though it still exhibits minor energy disturbances. In contrast, STFT, CWT, and SBCT yield lower SSIM values, indicating greater distortion and blurring in their TFRs. GLCT, which records the lowest SSIM, further confirms its severe energy dispersion and inability to accurately extract fault characteristic frequencies.

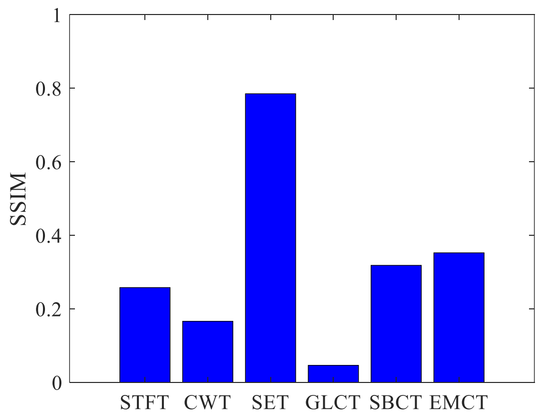

Figure 16. SSIM comparison of different TFR methods with LESSECT as the reference

In summary, the results demonstrate that LESSECT effectively processes tightly spaced non-proportional signals, capturing IF components with improved clarity and energy concentration. Its advantages are further supported by the lowest Rényi entropy and higher SSIM values, highlighting its potential for more accurate fault diagnosis in complex vibration signals.

5.3. Wind energy turbine planetary gear system evaluation

For the third dataset, the experimental setup and gear system structure are shown in Figure 17(a) and Figure 17(b), respectively. The system consists of a speed-increasing gearbox, a decelerating gearbox, a load system, a cooling unit, a frequency controller, and a drive motor. Both gearboxes on the test bench share the same design, incorporating two dual-stage fixed-axis gear assemblies and a single-stage planetary gear mechanism. In the dual-stage fixed-axis gear system, the tooth counts are as follows: 73 for the input stage, 21 for the intermediate stage, 66 for the second intermediate stage, and 23 for the output stage. The planetary gear mechanism consists of a central gear, three planetary gears, and a ring gear, with tooth counts of 17, 79, and 31, respectively .

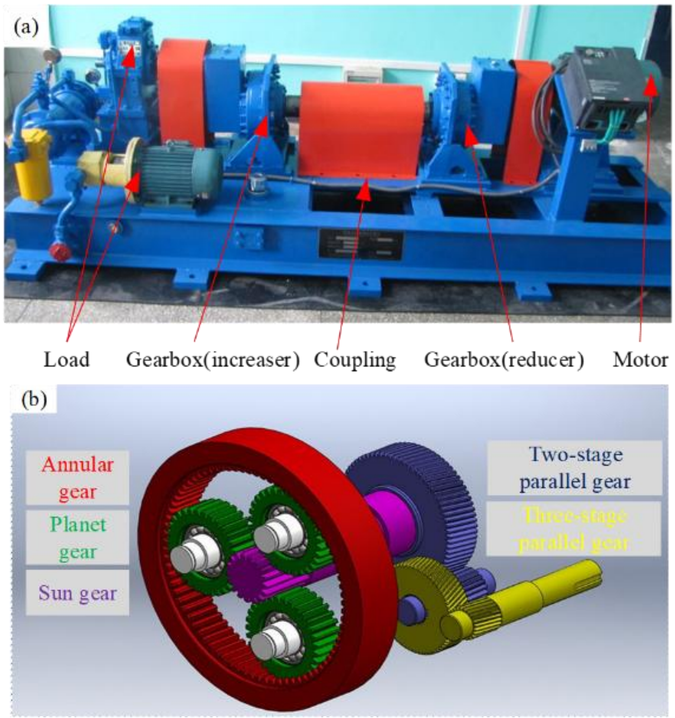

Figure 17. The wind turbine gearbox system: (a) Experimental setup; (b) Gearbox configuration.

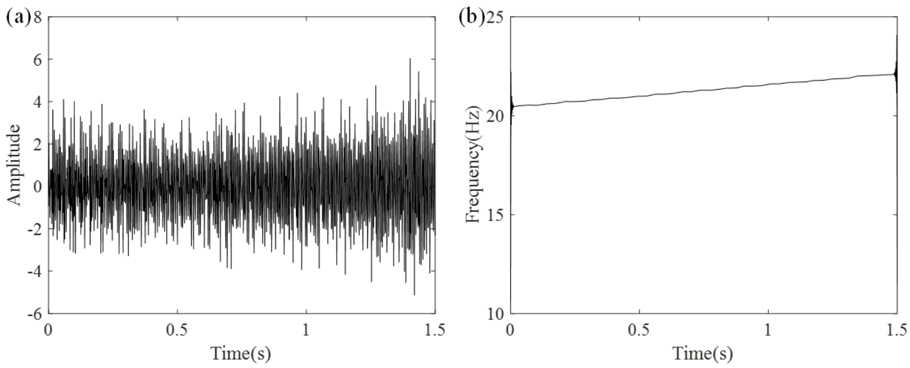

Figure 18. Vibration Signal from the Speed-Increasing Gearbox: (a) Waveform; (b) RF

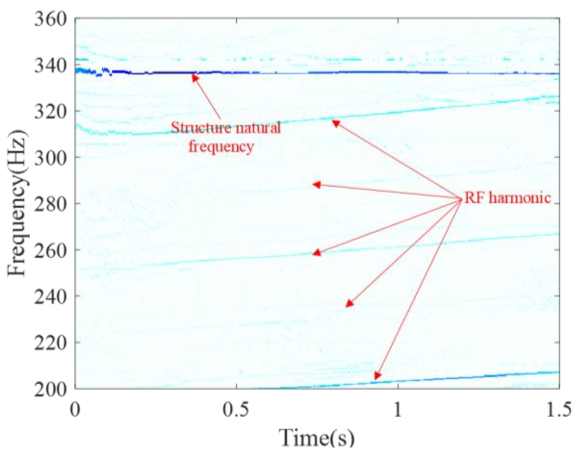

Figure 19. The LESSECT-derived TFR for the oscillation data from the speed-increasing gearbox.

The test system is driven by a motor regulated by a variable frequency drive, which supplies high-pressure fluid to the load system to simulate operational conditions. A 3056B1 accelerometer is mounted on the acceleration gearbox to capture vibration data. To analyze the vibration signal, the original signal is downsampled to 720 Hz, covering a duration of 1.5 s. Figure 18(a) and Figure 18(b) illustrate the signal waveform and the variation in rotational frequency, respectively.

Table 6. Rényi Entropy Comparison of 7 TFA Methods.

method	STFT	CWT	SET	GLCT	SBCT	EMCT	LESSECT
Rényi entropy	16.2471	16.5834	13.9578	18.5285	14.8585	16.2209	11.2064

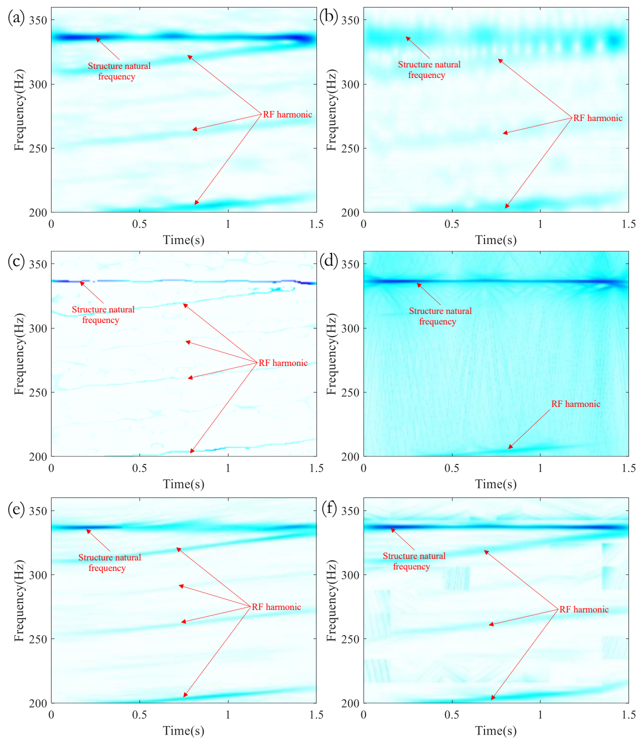

Figure 20. The TFR outcomes for the acceleration gearbox's vibration signal: (a) STFT; (b) CWT; (c) SET; (d) GLCT; (e) SBCT; (f) EMCT.

Figure 19 presents the TFR obtained using LESSECT with a window length of 450. Several characteristic frequency trajectories of physical significance are clearly distinguishable, including the system's inherent frequencies and their harmonic orders [36]. To further evaluate the effectiveness of LESSECT, its TFR is compared with those generated by STFT, CWT, SET, GLCT, SBCT, and EMCT. As shown in Figure 20(a)–Figure 20(f), most alternative methods fail to fully and accurately capture the key frequency components and structural natural frequency trajectories. Specifically, GLCT identifies only the structural natural frequencies, failing to extract resonance harmonics. CWT produces highly blurred TFRs with significant energy leakage. STFT, SBCT, and EMCT reveal partial rotational frequency harmonics but suffer from varying degrees of energy leakage. Although SET extracts resonance harmonic components to some extent, the IF trajectories of each harmonic order are severely distorted. Overall, these methods exhibit energy dispersion and fail to provide an accurate TFR.

To quantify the energy concentration of each method, Table 5 presents the Rényi entropy values. A lower entropy value indicates a more concentrated energy distribution. LESSECT achieves the lowest entropy, demonstrating its superior ability to concentrate TF energy. In contrast, other methods, such as GLCT and CWT, exhibit higher entropy, indicating more dispersed energy distributions.

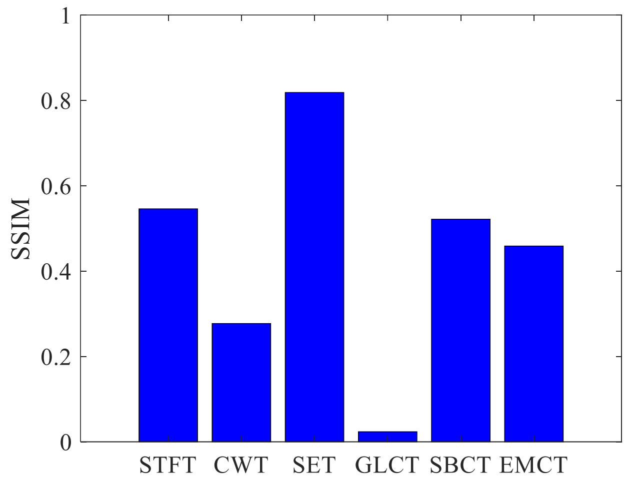

Figure 21. SSIM comparison of different TFR methods with LESSECT as the reference.

To further assess the quality of the TFRs, SSIM is employed to compare the TFRs obtained from different methods against the LESSECT-generated TFR. SET achieves the highest SSIM among the alternative methods, indicating a relatively higher structural similarity. However, other methods, particularly GLCT and CWT, yield significantly lower SSIM scores, suggesting a substantial loss of structural integrity. Figure 21 visually presents the SSIM comparison across different methods. These results reaffirm the advantages of LESSECT in preserving structural details and achieving a more accurate TFR.

In conclusion, LESSECT outperforms other TFA methods in accurately capturing IF components with enhanced clarity and energy concentration. Its effectiveness is validated by the lowest Rényi entropy and the highest structural similarity to an ideal TFR, further demonstrating its potential in handling complex, non-stationary signals.

6. Conclusion

Under dynamic conditions, vibration signals in rotating machinery exhibit non-proportional and highly asynchronous behaviors across different components. These characteristics lead to severe energy leakage in existing TFA methods, making it difficult to accurately capture all key frequency trajectories. Such inaccuracies can compromise the reliability of fault diagnosis and condition monitoring in rotating machinery systems. To address these challenges, this study introduces a novel TFA method, LESSECT. This approach constructs a second-order nonlinear chirplet basis function, incorporating Rényi entropy to extract multiple CRs at the same time center, thereby effectively matching all frequency components. The IF ridges are subsequently re-extracted based on the generated TFR. By redistributing energy to the TF positions corresponding to the target components, LESSECT significantly reduces interference from non-target signals and enhances TFR readability. Through evaluations on one synthetic dataset and three sets of vibration measurements, along with comparisons against six additional TFA techniques, LESSECT demonstrates its capability to accurately identify closely spaced and non-proportional IF components while producing a TFR with higher energy concentration. This not only improves fault detection accuracy but also enhances system reliability through precise state estimation.

Given its ability to achieve high energy concentration and accurately capture IF components in complex non-stationary signals, LESSECT holds significant potential for industrial applications. In rotating machinery fault diagnosis, precise TFR representation plays a crucial role in detecting early-stage faults and distinguishing closely spaced frequency components. LESSECT's superior performance in these aspects can contribute to more reliable condition monitoring and predictive maintenance strategies, reducing unexpected downtime and maintenance costs. Additionally, its robustness in handling non-proportional and highly asynchronous signals makes it well-suited for diagnosing faults in complex gear transmission systems, rolling bearings, and other critical rotating components under variable operating conditions. These advantages indicate that LESSECT can serve as a valuable tool for improving fault detection accuracy and ensuring the operational reliability of industrial equipment.

Despite its advantages, LESSECT has certain limitations. It faces challenges in extracting weak fault features at early degradation stages due to the inherently low energy of these components, which may affect early fault detection sensitivity. Additionally, compared to conventional TFA methods, LESSECT requires a higher computational cost, which may limit its feasibility for real-time industrial applications. Future research will focus on improving the method's capability in weak fault feature extraction and optimizing the algorithm's computational efficiency, making it more adaptable for real-time condition monitoring and large-scale industrial deployment.

Reference

1. Wei Y, Li Y, Xu M, Huang W. A review of early fault diagnosis approaches and their applications in rotating machinery. Entropy. 2019;21(4):409. https://doi.org/10.3390/e21040409.
2. Liu D, Cui L, Wang H. Rotating machinery fault diagnosis under time-varying speeds: A review. IEEE Sensors J. 2023. https://doi.org/10.1109/JSEN.2023.3326112.
3. Zhu X, Sun J, Hu H, Li C, A Semi-Supervised Siamese Network for Complex Aircraft System Fault Detection with Limited Labeled Fault Samples, Eksploatacja i Niezawodnosc – Maintenance and Reliability 2023: 25(4) http://doi.org/10.17531/ein/174382.
4. Su Z, Hua Z, Hu D, Zhao M, Research on Equipment Reliability Modeling and Periodic Maintenance Strategies in Dynamic Environment, Eksploatacja i Niezawodnosc – Maintenance and Reliability 2025: 27(1) http://doi.org/10.17531/ein/192163.
5. Zhang X, Zhao J. Compound fault detection in gearbox based on time synchronous resample and adaptive variational mode decomposition. Eksploatacja i Niezawodnosc – Maintenance and Reliability 2020; 22 (1): 161–169, http://dx.doi.org/10.17531/ein.2020.1.19.
6. Huang R, Xia J, Zhang B, Chen Z, Li W. Compound fault diagnosis for rotating machinery: State-of-the-art, challenges, and opportunities.

J Dyn Monit Diagn. 2023;13-29. https://doi.org/10.37965/jdmd.2023.152.

7. Tiboni M, Remino C, Bussola R, Amici C. A review on vibration-based condition monitoring of rotating machinery. Appl Sci. 2022;12(3):972, https : //doi.org/10.3390/app12030972.
8. Lu S, Lu J, An K, Wang X, He Q. Edge computing on IoT for machine signal processing and fault diagnosis: A review. IEEE Internet Things J. 2023;10(13):11093-11116, https://doi.org/10.1109/JIOT.2023.3239944.
9. Zhang J, Kong Y, Chen Z, Han, T, Han, Q, Dong, M, Chu, F. CBAM-CRLSGAN: A novel fault diagnosis method for planetary transmission systems under small samples scenarios. Measurement, 2024;234:114795, https://doi.org/10.1016/j.measurement.2024.114795.
10. Kong, Y, Han, Q, Chu, F, Qin, Y, Dong, M. Spectral ensemble sparse representation classification approach for super-robust health diagnostics of wind turbine planetary gearbox. Renewable Energy. 2023;219:119373, https://doi.org/10.1016/j.renene.2023.119373.
11. Lin C, Kong Y, Han Q, Zhang X, Qi J, Rao M, et al. An unsupervised multi-level fusion domain adaptation method for transfer diagnosis under time-varying working conditions. Mech Syst Signal Process. 2025;228:112458, https://doi.org/10.1016/j.ymssp.2025.112458.
12. Li, X, Yu, T, Zhang, F, Huang, J, He, D, Chu, F. Mixed style network based: A novel rotating machinery fault diagnosis method through batch spectral penalization. Reliability Engineering & System Safety, 2024;255:110667, https://doi.org/10.1016/j.ress.2024.110667.
13. Li X, Yu T, Zhang F, Huang J, He D, Chu F. Mixed style network based: A novel rotating machinery fault diagnosis method through batch spectral penalization. Reliab Eng Syst Saf. 2025;255:110667, https://doi.org/10.1016/j.ress.2024.110667.
14. Zhao D, Cai W, Cui L. Multi-perception Graph Convolutional Tree-embedded Network for Aero-engine Bearing Health Monitoring with Unbalanced Data[J]. Reliability Engineering & System Safety, 2025: 110888.
15. Liu T, Yan S, Zhang W. Time-frequency analysis of nonstationary vibration signals for deployable structures by using the constant-Q nonstationary Gabor transform. Mech Syst Signal Process. 2016;75:228-244. https://doi.org/10.1016/j.ymssp.2015.12.015.
16. Yang Y, Peng Z, Zhang W, et al. Parameterised time-frequency analysis methods and their engineering applications: A review of recent advances. Mech Syst Signal Process. 2019;119:182-221. https://doi.org/10.1016/j.ymssp.2018.07.039.
17. Portnoff M. Time-frequency representation of digital signals and systems based on short-time Fourier analysis. IEEE Trans Acoust Speech Signal Process. 1980;28(1):55-69. https://doi.org/10.1109/TASSP.1980.1163359.
18. Daubechies I. The wavelet transform, time-frequency localization and signal analysis. IEEE Trans Inf Theory. 1990;36(5):961-1005. https://doi.org/10.1109/18.57199.
19. Boashash B, Black P. An efficient real-time implementation of the Wigner-Ville distribution. IEEE Trans Acoust Speech Signal Process. 1987;35(11):1611-1618. https://doi.org/10.1109/TASSP.1987.1165070.
20. Mann S, Haykin S. The chirplet transform: Physical considerations. IEEE Trans Signal Process. 1995;43(11):2745-2761. https://doi.org/10.1109/78.482123.
21. Yu G, Zhou Y. General linear chirplet transform. Mech Syst Signal Process. 2016;70-71:958-973. https://doi.org/10.1016/j.ymssp.2015.09.004.
22. Guan Y, Liang M, Necsulescu DS. Velocity synchronous linear chirplet transform. IEEE Trans Ind Electron. 2018;66(6):6270-6280. https://doi.org/10.1109/TIE.2018.2873520.
23. Li M, Wang T, Chu F, et al. Scaling-basis chirplet transform. IEEE Trans Ind Electron. 2020;68(9):8777-8788. https://doi.org/10.1109/TIE.2020.3013537.
24. Czarnecki, K, Fourer, D, Auger, F, Rojewski, M. A fast time-frquency multi-window analysis using a tuning directional kernel. Signal Prcess. 2018.147:110-119. https://doi.org/10.1016/j.sigpro.2018.01.019.
25. Miao Y, Sun H, Qi J. Synchro-compensating chirplet transform. IEEE Signal Process Lett. 2018;25(9):1413-1417. https://doi.org/10.1109/LSP.2018.2858018.
26. Zhang D, Feng Z. Proportion-extracting chirplet transform for nonstationary signal analysis of rotating machinery. IEEE Trans Ind Informatics. 2022;19(3):2674-2683. https://doi.org/10.1109/TII.2022.3185771.
27. Auger F, Flandrin P. Improving the readability of time-frequency and time-scale representations by the reassignment method. IEEE Trans Signal Process. 1995;43(5):1068-1089. https://doi.org/10.1109/78.382394.
28. Zhao, D, Huang, X, Cui, L. Horizontal reassigning transform for bearing fault impulses characterizing. IEEE Sensors Journal. 2023;24(2):1837-1846. https://doi.org/10.1109/JSEN.2023.3337137.

29. Daubechies I, Lu J, Wu HT. Synchrosqueezed wavelet transforms: An empirical mode decomposition-like tool. Appl Comput Harmonic Anal. 2011;30(2):243-261. https://doi.org/10.1016/j.acha.2010.08.002.
30. Yu G, Yu M, Xu C. Synchroextracting transform. IEEE Trans Ind Electron. 2017;64(10):8042-8054. https://doi.org/10.1109/TIE.2017.2696503.
31. Holighaus, N, Průša, Z, Søndergaard, P. L. Reassignment and synchrosqueezing for general time–frequency filter banks, subsampling and processing. Signal Processing. 2016;125:1-8. https://doi.org/10.1016/j.sigpro.2016.01.007.
32. He Y, Hu M, Jiang Z, Feng K, Ming X. Local maximum synchrosqueezes from entropy matching chirplet transform. Mech Syst Signal Process. 2022;181:109476. https://doi.org/10.1016/j.ymssp.2022.109476.
33. Wu T, Zhang W, Zhang B, Luo H. Application of multi-base fusion generalized chirplet basis transform in vibration signal analysis of multiple rotor rotating machinery. Mech Syst Signal Process. 2023;185:109792. https://doi.org/10.1016/j.ymssp.2022.109792.
34. Randall RB, Antoni J. Rolling element bearing diagnostics-A tutorial. Mech Syst Signal Process. 2011;25(2):485-520. https://doi.org/10.1016/j.ymssp.2010.07.017.
35. Huang H, Baddour N. Bearing vibration data collected under time-varying rotational speed conditions. Data Brief. 2018; 21:1745-1749. https://doi.org/10.1016/j.dib.2018.11.019.
36. Z Feng, M J Zuo, Vibration signal models for fault diagnosis of planetary gearboxes, J. Sound Vib. 331 (2012) 4919–4939, https://doi.org/10.1016/j.jsv.2012.05.039.

Nomenclature and Abbreviations

TFA	Time-frequency analysis	SST	Synchro-squeezing transform
IF	Instantaneous frequency	SET	Synchro-extracting transform
TFR	Time-frequency representation	SRT	Synchronized Reassignment Transform
CR	Chirp rate	EMCT	Entropy Matching Chirplet Transform
STFT	Short-time Fourier transform	GCBT	Generalized Chirplet basis transform
CWT	Continuous wavelet transform	RF	Rotational frequency
WVD	Wigner-Ville Distribution	TFD	Time-frequency distribution
CT	Chirplet transform	TF	Time-frequency
GLCT	General linear Chirplet transform	IP	Instantaneous phase
VSLCT	Velocity synchronous linear Chirplet transform	IA	Instantaneous amplitude
SBCT	Scaling-basis Chirplet transform	SEO	Synchro-extracting operators
CMCT	Component matching Chirplet transform	ESBCT	entropy- SBCT
SSCT	Slope-Synchronized Chirplet Transform	FCF	fault characteristic frequencies
PECT	Proportional Extraction Chirplet Transform	RF	Rotation frequency
RM	reassignment		